Composites Science and Technology 219 (2022) 109241

Contents lists available at ScienceDirect

Composites Science and Technology

journal homepage: www.elsevier.com/locate/compscitech

Charge transport and space charge dynamics in EPDM/2D-nanoclay composite dielectrics

Mohamadreza Arab Baferani, Chao Wu, Yang Cao *

Electrical and Computer Engineering, University of Connecticut, Storrs, CT, 06269, USA

ARTICLE INFO

Keywords:
Charge transport
Electrical conductivity
EPDM
2D-nanoclay
Space charge dynamics
Dielectric response

ABSTRACT

Composite dielectrics with two types of 2D-nanoclays (i.e., Kaolinite and Talc) incorporated in ethylene propylene diene monomer (EPDM) as the polymer matrix exhibit distinctly different electrical performances for high-voltage direct current (HVDC) cable insulations. This study investigated electrical conductivity and space charge as the key electrical characteristics of DC cable insulation in conjunction with dielectric spectroscopies. The findings of this study revealed that the composite dielectric with Talc 2D-nanoclays significantly suppressed space charge and thus minimized electric field distortion to less than 9% under 20 kV/mm at both measured temperatures of 25 °C and 50 °C with thermal gradient. In addition, the activation energy of electrical conductivity for the composite dielectric with Talc 2D-nanoclays is 0.45 eV which is notably lower than that of the composite dielectric with Kaolinite 2D-nanoclays, 0.95 eV. Based on the experimental results, the microstructural characteristics of composite dielectrics were discussed to provide insights into charge transport and space charge dynamics in the composite dielectrics. The charge transport mechanism attributed to the electronic and ionic conduction was explained, and the reasons for space charge accumulation were discussed. The larger interfacial area of 2D-nanoclay particles, the uniform and oriented distribution of 2D platelet-like nanoclay, and the smaller difference between the bandgap of polymer and 2D-nanoclay particles contribute to controlling the charge transport and suppressing the space charge accumulation in the composite dielectrics. Charge dynamics from the dielectric spectroscopy based on the Dissado-Hill model analysis confirms the explained mechanism.

1. Introduction

Large scale offshore wind farms successfully developed in Europe are rapidly expanding around the world. In 2020, the Global Wind Energy Council (GWEC) predicted that the global offshore capacity will reach over 234 GW by 2030. This would add more than 205 GW of new offshore wind farms to the 2019 capacity of 29.1 GW with new installations mainly led by the explosive growth in Asia-Pacific regions as well as the continuous significant growth in Europe [1]. The wind turbines of the offshore wind farms can provide a reliable power generation in regions with strong and steady wind power with a lower acoustic and visual impact on people's life compared with onshore wind farms [2]. Transmission of the generated power can be accomplished with both high-voltage alternating current (HVAC) and high-voltage direct current (HVDC) cabling. However, with the trend of increased distance between offshore wind farms and onshore grid, utilizing HVDC cabling becomes more cost-effective.

Developing high-quality HVDC cable insulations requires delicate tuning of the electric field across the insulation. The electric field distribution under DC voltage in the cylindrical cable insulation initiates with the Laplacian electric field distribution; however, the thermal gradient (TG) across the insulation and the change of the electrical conductivity because of its temperature dependence under loading conditions will lead to the phenomenon of electric field inversion across the dielectric [3]. In addition, the electric field distribution across a DC cable insulation is affected and often distorted by the accumulation of space charge. Therefore, controlled electrical conductivity and highly suppressed space charge accumulation are desired for tailoring the electric field across the cable insulation under DC.

The mass-impregnated (MI) insulations have been used traditionally for DC cabling systems with line-commutated converter (LCC) schemes. The MI insulations produced by a lapping process could be considered as a layered *composite structure* with excellent performance under polarity reversal condition which is essential for changing the direction of power flow in LCC systems. With the rapid expansion in the adoption of DC cabling systems with voltage sourced converter (VSC) free from the need

---

* Corresponding author.
E-mail address: yang.cao@uconn.edu (Y. Cao).

https://doi.org/10.1016/j.compscitech.2021.109241
Received 31 October 2021; Received in revised form 16 December 2021; Accepted 20 December 2021

of the polarity reversal, special grades of extruded HVDC cables based on the cross–linked polyethylene (XLPE) can now be used. Compared with MI insulation cables, the XLPE insulations are lighter, less expensive, and less harmful for the environment compared with MI insulation cables, and can be manufactured by continuous extrusion process and conveniently extended during installation by oil-free pre-molded joints. However, DC cables with XLPE insulation are only applicable for the VSC systems [4]. Therefore, there still exists the need for insulation with the advantages of both MI and polymeric insulations, i.e., an extrudable insulation that is compatible with polarity reversal.

In comparison with XLPE, ethylene propylene rubber (EPR) is a promising polymer for high-voltage applications because of its higher flexibility, more stable mechanical properties with temperature, and lower thermal expansion [5,6]. However, EPR is amorphous and does not have a proper mechanical performance such as toughness. Furthermore, the pure EPR shows a high amount of space charge accumulation and high dependency of electrical conductivity on electric field [7]. The composite dielectrics with the addition of inorganic two-dimensional (2D) nanoclays to polymer can regulate the mechanical and electrical properties of the polymer due to the combined excellent performances of organic and inorganic materials [8]. For example, the incorporation of aligned nanoplatelet montmorillonite into polyethylene yields an independent and complementary enhancement of the breakdown strength beyond any improvements related to the crystal orientation [9,10].

The 2D-nanoclays are among the favorable fillers for the larger interfacial area compared with the three-dimensional (3D) nanoparticles like spherical particles. Moreover, clays are abundant as natural minerals, so they can be produced on a large scale. The 2D-nanoclays have a great capability in upgrading the mechanical properties of composite dielectrics [11,12]. More importantly, the engineered presence of 2D-nanoclays in dielectrics has exhibited great improvement in the suppression of space charge accumulation. In addition to the chemical, physical, and morphological characteristics of inorganic fillers, the key to achieve the improved electrical performance for the composite dielectrics is the uniform distribution of nanoparticles and being free from aggregation [13,14]. As the larger interfacial area and the smaller size of the nanoparticles make them easier to aggregate, close attention should be paid to the distribution of the nanoparticles in composite dielectrics for HVDC cable applications [15,16].

A fundamental understanding of charge transport mechanisms can rationally guide the targeted improvement of the engineering process of composite dielectrics for HVDC cable insulation. In polymeric insulations, the charge transport mechanism has been studied for years, and some numerical models have been developed to describe the charge transport and accumulation phenomena [17,18]. However, the charge transport under DC electric field in composite dielectrics is still not clear due to the complicated interfacial states between nanoparticles and polymer matrix. There are some models that emphasize the interface between polymer chains and nanoparticles. Lewis in 2004 introduced the concept of the interface in nanometric dielectrics and highlighted the importance of interface in dielectric nanocomposites [19]. In 2005, Tanaka established a Multi-core model to describe the behavior of nanoparticles interface for spherical nanoparticles and defined three layers between nanoparticles and polymer chains [20]. Since then, other researchers tried to shed light on the mechanisms related to electrical properties of dielectrics with incorporated nanoparticles [21–24]. Nonetheless, the way that nanoparticles affect charge transport and contribute to the modification of DC electrical conductivity and space charge accumulation has been given little attention. This work aims to investigate the impact of the 2D-nanoclays on charge transport and accumulation in composite polymeric dielectrics and elucidate the mechanism therein to guide the design of the next generation of DC cable insulation. Focusing on the charge transport dynamics and considering the well-known models regarding nanodielectrics such as the Lewis model and the Multi-Core model of Tanaka, this study discusses the experimental results of composite dielectrics with ethylene propylene diene monomer (EPDM) as the base polymer matrix and two different 2D-nanoclays, Kaolinite and Talc. Space charge and electrical conductivity as two major electrical properties of dielectrics used in DC cable insulations were measured, and the results were explained. The dielectric spectroscopy analyzed with the Dissado-Hill dielectric response theory was utilized to support the discussion.

2. Experiments

2.1. Sample preparation

Two different 2D-nanoclays which are Kaolinite, an aluminum silicate, and Talc, a magnesium silicate, were incorporated in EPDM polymer matrix with a constant 40% weight ratio based on the total weight of the composite dielectric followed with peroxide crosslinking. The Kaolinite is the Translink from BASF and the Talc is a treated Talc. The materials were mixed and prepared using the melt blending method with roller style mixing blades. The model EPR composite materials were provided by the EPR consortium including companies of Kerite, Okonite, Electrical Cable Compounds, Lion Elastomers, and ExxonMobil. The prepared materials were hot-pressed at 120 °C with 9 tones pressure to make the flat plaque samples with a desired thickness. The desired thickness of the samples for electrical conductivity and space charge measurement is 250 μm. Then, the samples were cross-linked at 165 °C under 5 tones pressure. All the samples were degassed for 5 days at 80 °C in a vacuum oven. The first sample is the EPDM polymer with Kaolinite 2D-nanoclays which is named EPDM1. The second sample has Talc 2D-nanoclay particles in the EPDM polymer labeled as EPDM2. Differential scanning calorimetry (DSC) scans with 10 °C/min rate of heat flow were used, and the glass transition of the pure EPDM and the EPDM filled with 2D-nanoclays was observed to be ~ -50 °C. Therefore, adding the 2D-nanoclays does not appear to change the glass transition temperature of the EPDM.

A ThermoFisher Teneo scanning electron microscope (SEM) was used to investigate the 2D-nanoclays distribution in the EPDM matrix across the samples. The samples were fractured in liquid nitrogen and then coated with a 2 nm layer of Au/Pd to avoid e-beam charging. As demonstrated in Fig. 1(a), the 2D-nanoclay particles in EPDM1 were aggregated and formed the bulb-like micro particles. The size and distribution of particles in EPDM1 are not uniform. Conversely, the 2D platelet-like Talc particles were distributed uniformly in the polymer matrix without significant aggregation in EPDM2 as shown in Fig. 1(b). It can be observed that EPDM2 has a textured structure with clear orientation of the 2D-nanoclay particles.

The X-ray pole figure technique was utilized to study the orientation of the 2D platelet-like nanoclay in EPDM2 [25]. The high-resolution X-ray diffractometer (XRD) Rigaku SmartLab was applied to record the pole figure. As the first step, the X-ray diffraction (XRD) spectroscopy of EPDM2 was measured as shown in Fig. 2(a). The XRD reveals the sharp diffraction peaks at $2\theta = 9.4^\circ$, 19°, 28.6° and 38.5° and a wide amorphous peak at around 21° related to the amorphous EPDM. The sharp diffraction peaks are related to the Talc 2D-nanoclay particles orientation and assigned to (002), (004), (006), and (008), respectively. All these peaks indicate the orientation of the particles parallel to the surface of the sample. Therefore, only the preferred orientation of (002) with the peak at $2\theta = 9.4^\circ$ was chosen for more detailed texture analysis. Fig. 2(b) presents the flat 2D pole figure related to the diffraction angle of $2\theta = 9.4^\circ$. The color map shows the diffracted intensity distribution on the surface measured at a constant distance from the origin of the coordinate system. In this figure, α is the tilt angle between the diffraction vector and the surface of the sample, and β is the rotational angle of the diffraction vector around the normal vector perpendicular to the surface. As it can be observed, the maximum pole density is reached at $\alpha = 90^\circ$ corresponding to the condition with the diffraction vector normal to the surface. This maximum pole density decreases

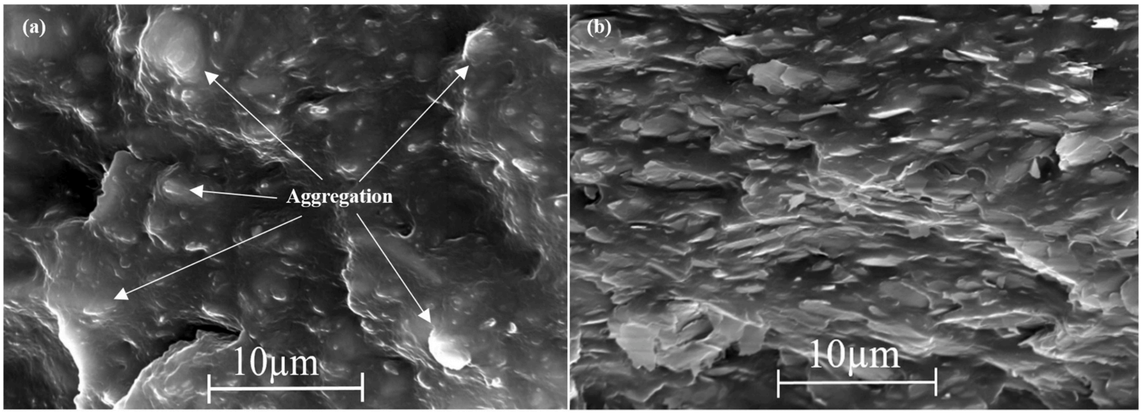

Fig. 1. SEM image of cross section (a) EPDM1 and (b) EPDM2.

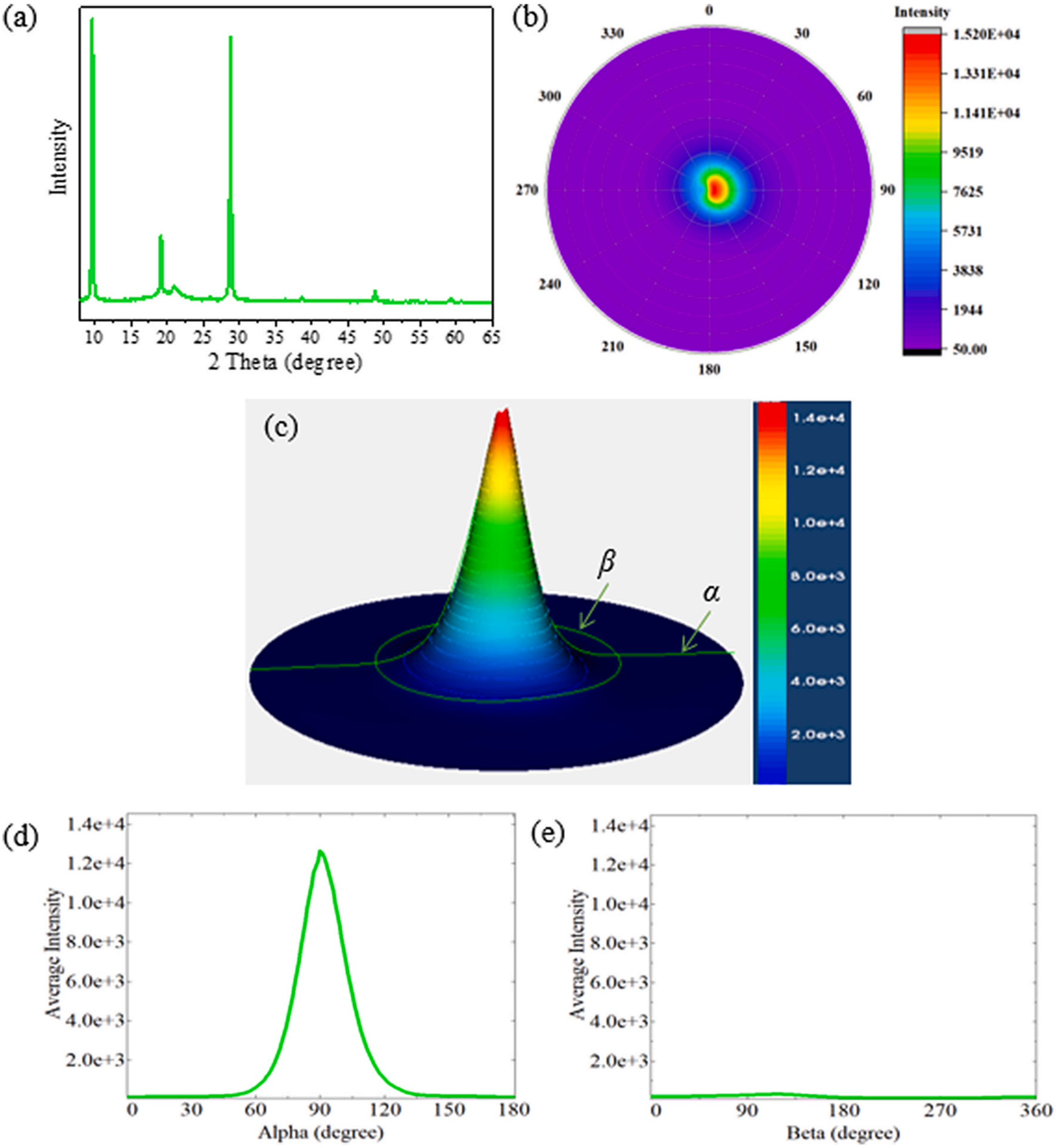

Fig. 2. (a) the X-ray diffraction peaks, (b) the flat 2D pole figure, (c) the raised pole figure, (d) average intensity with changing α at $\beta = 0^\circ$, and (e) the average intensity with changing β at $\alpha = 45^\circ$ for EPDM2.

quickly when the diffraction vector moves parallel to the surface which are $\alpha = 0^\circ$ and $\alpha = 180^\circ$. Fig. 2(c) presents the raised form of the pole figure for EPDM2. Two green lines in this figure demonstrate the change of angles α and β. The change of α angle at the constant $\beta = 0^\circ$ has been shown in Fig. 2(d). Obviously, the α peak is located at exactly 90°, as expected from the results in Fig. 2(b) and (c). The evolution of angle β, from $\beta = 0^\circ$ to $\beta = 360^\circ$ in completion of a whole circle, at the fixed $\alpha = 45^\circ$, can be observed in Fig. 2(e). The diffracted intensity does not change with β parameter. These results clearly confirm the high degree of orientation of the 2D-nanoclay particles in EPDM2 in parallel with the surface of the film sample.

2.2. *Electrical conductivity*

The DC electrical conductivity of the samples was measured using a three-terminal (two terminals plus a guard) sample holder built based on the ASTM 257 standard. The electrodes are circular and made of copper with radius of 10 mm as the inner electrode, 15 mm as the inner radius of guard, and 18 mm as the outer radius of guard. The specimens were prepared with the thickness of 250 μm and 10 cm × 10 cm surface area to reduce the possibility of surface discharge. An oven was utilized to create the stable desired temperature in the range of 30–90 °C. A Keithey 6514 electrometer was used to record the polarization current for 2000 s. The average of the measured data in the range of 1900–2000 s was used to calculate the current density and the electrical conductivity.

The electrical conductivity of the samples was measured under electric fields of 10, 20, 30, and 40 kV/mm at 30, 50, 70, and 90 °C. These electric fields and temperatures cover the normal operation ranges of the conventional DC cable insulation. In general, the conductivity of the samples enhances with temperature and electric field as shown in Fig. 3. With the increase of electric field, the conductivity of EPDM1 changes more notably compared with EPDM2 at 30 and 50 °C. For instance, the conductivity of EPDM1 enhanced with electric field rise around one order of magnitude from 7×10^{-16} (S/m) to 3×10^{-15} (S/m) at 30 °C; however, the conductivity stayed stable with electric field, i.e., from 3.8 to 4.8×10^{-15} (S/m), for EPDM2.

At the step of temperature rise from 50 to 70 °C, both samples have higher electrical conductivity enlargement compared with the step of 30–50 °C. For example, it increased from 1.8×10^{-15} (S/m) to 9×10^{-15} (S/m) for EPDM1 and from 8.6×10^{-15} (S/m) to 4.8×10^{-14} (S/m) for EPDM2 under 10 kV/mm. Overall, the electrical conductivity of EPDM2 is higher than EPDM1 under the same electric field and temperature. However, compared with EPDM1, the dependency of conductivity on the electric field is less in EPDM2, especially at lower temperatures of 30 and 50 °C. Although the conductivity of EPDM1 is clearly lower than EPDM2 at 10 and 20 kV/mm, because of the higher dependency of conductivity on the electric field in EPDM1, its conductivity augments and reaches close to that of EPDM2 at 30 and 40 kV/mm.

The dependency of conductivity on temperature at a given electric field follows the Arrhenius function as (1):

$$\sigma(T) = \sigma_0 \, exp\boxed{f_0}\left(\frac{-\varphi}{kT}\right) \tag{1}$$

where σ_0 is the asymptotic value of the DC conductivity at infinite temperature (S/m), φ is the activation energy (eV), k is the Boltzmann's constant, 8.617×10^{-5} (eV/K), and T is the absolute temperature (K) [26]. The obtained activation energy for the conduction process represents a measure of the hindrance against charge transport. The activation energy of EPDM1 and EPDM2 at 10 kV/mm is 0.95 eV and 0.45 eV, respectively, and the fitted amount of σ_0 is 1.81×10^{2} (S/m) for EPDM1 and 2.08×10^{-7} (S/m) for EPDM2. These results will be discussed in Section 3.1.

2.3. *Space charge characterization*

The space charge distribution was measured by a Pulsed Electroacoustic (PEA) instrument. Samples with the thickness of ~250 μm were metalized on both sides with 60/40% Au/Pd with a sputtering coater. The details of the PEA method and measurement procedure can be found in previous publications [27–29]. The space charge distribution across the samples was mapped as shown in Fig. 4. The color map demonstrates the time evolution of space charge distribution, with the vertical axis for position across the sample in per unit (P.U.), the horizontal axis for the duration of space charge measurement in minutes, and the color for charge density in C/m^3. The space charge distribution has been measured under 20 kV/mm at 25 °C and with a thermal gradient (TG) of 1 °C/mm at 50 °C. For a power cable under typical load conditions, a temperature gradient of 5–15 °C is developed with the surface temperature of the cable reaching ~50 °C. For an actual 150 kV HVDC cable with the insulation thickness of ~15 mm, a thermal gradient per unit thickness of ~1 °C/mm is developed. The 1 °C/mm TG is not the worst-case condition, however; it is one of the relevant and representative conditions for characterizing the designed material for the HVDC power cable under normal load operation. The direction of TG is parallel to the applied electric field with the higher temperature at the cathode and the lower temperature at the anode. Thin film electric heaters were utilized to heat up the bottom aluminum electrode to generate sufficient and laterally uniform TG across the sample. The temperature of bottom electrode could be controlled by changing the heater current. A feedback loop was provided for proportional-integral-derivative (PID) temperature control by deploying a resistor temperature detector (RTD) sensor to monitor the temperature on both the upper and lower surfaces of the specimen. In actual measurement, the total thickness of the sample plus

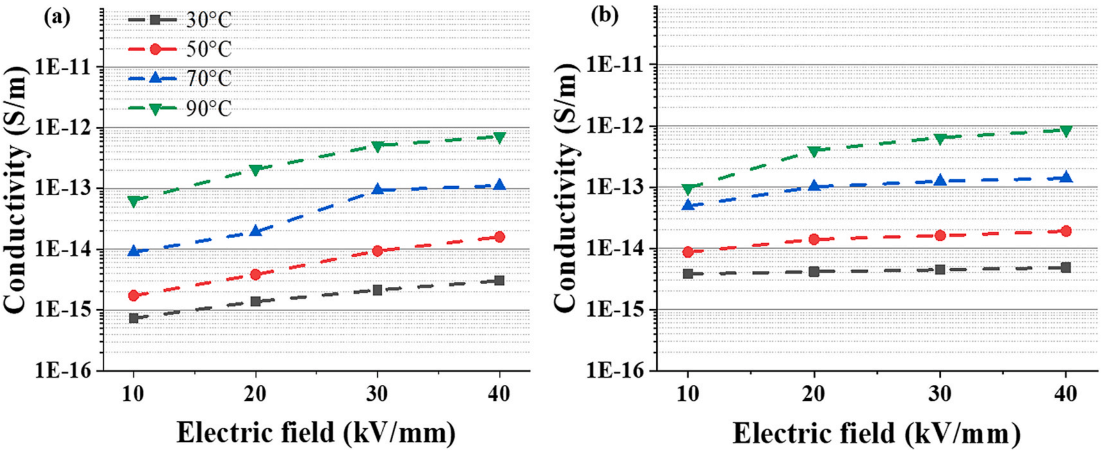

Fig. 3. Electrical conductivity at different electric fields and temperatures (a) EPDM1 and (b) EPDM2.

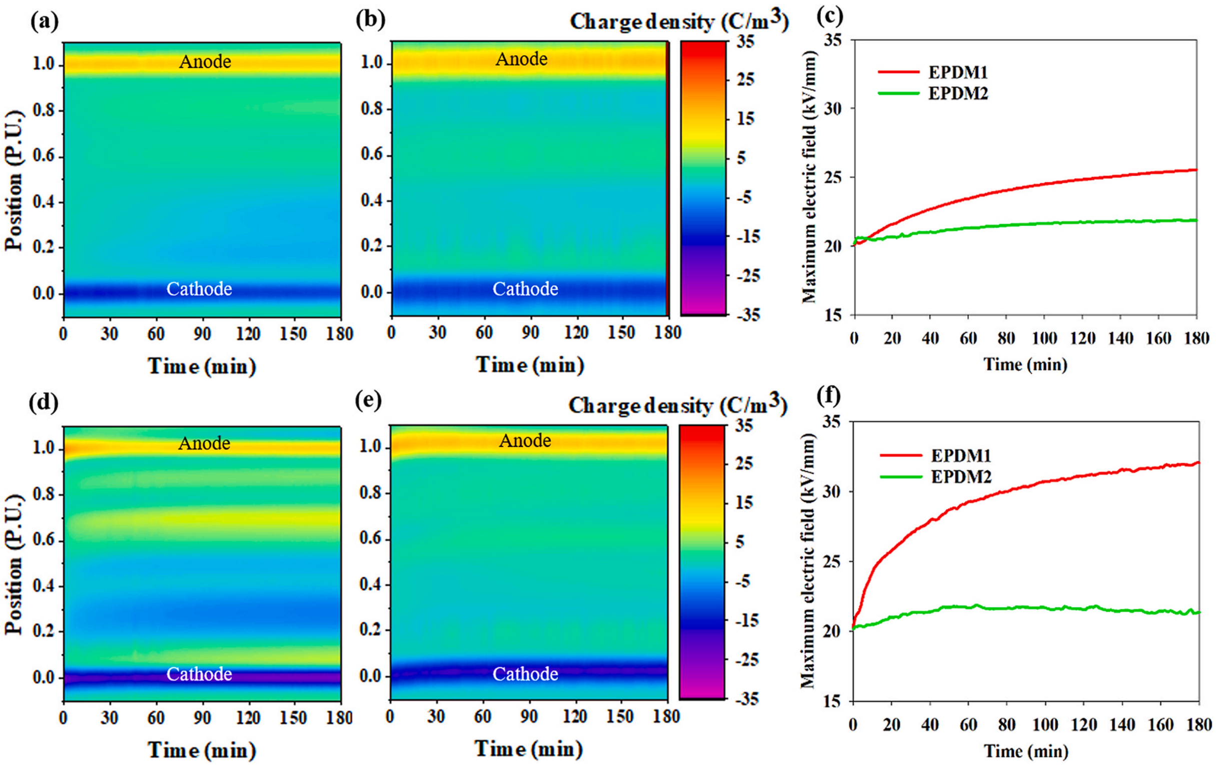

Fig. 4. At 25 °C: (a) charge density distribution for EPDM1, (b) charge density distribution for EPDM2, (c) maximum electric field distribution; at 50 °C with TG: (d) charge density distribution for EPDM1, (e) charge density distribution for EPDM2, and (f) maximum electric field distribution.

the semiconductor is ~1.2 mm. With a measured temperature drop of 1.2–1.3 °C across the sample plus the semiconductor, the desired TG of ~1 °C/mm is thus achieved. The PEA sample cell is housed in a thermostatic oven for ambient temperature adjustment [29].

As a function of time, for the sample EPDM1 as shown in Fig. 4(a), the accumulation of charge carriers near the cathode (at a position of 0.2 P.U.) and the anode (at a position of 0.7 P.U.) can be observed at 25 °C. The sample EPDM2 in Fig. 4(b) showed better performance without any significant accumulation of charge under the same electric field of 20 kV/mm and during the 180 min measurements at 25 °C. With the temperature rise to 50 °C and in the presence of TG, the charge accumulation for EPDM1 became worse. As demonstrated in Fig. 4(d), EPDM1 shows charge accumulation at different positions across the sample. At the positions of 0.3 P.U. close to the cathode and 0.7 P.U. close to the anode, accumulation of homo-polar charge became significant.

The space charge accumulation could modify the electric field distribution across the sample and cause the electric field distortion. Fig. 4 (c) and (f) depict the maximum electric field across samples during 180 min. At 25 °C, the maximum electric field for EPDM1 enhanced up to 25.5 kV/mm, whereas for EPDM2 it reached only 21.7 kV/mm. In other words, EPDM1 exhibits a 27.5% electric field enhancement, while EPDM2 only has 8.5% electric field enhancement. With the temperature rise to 50 °C and TG, the electric field distortion of EPDM1 had been worsened and enlarged to a maximum field of 31.9 kV/mm, which is 59.5% enhancement over the uniform electric field distribution of 20 kV/mm. On the other hand, EPDM2 at the same condition still has negligible electric field distortion with the maximum electric field of 21.8 kV/mm, i.e., a 9% electric field enhancement. It can be also seen that the maximum electric field reached a stable condition during the 180-min measurement for EPDM2. In contrast, the maximum electric field of EPDM1 increases markedly over the testing period of 180 min and would possibly enhance even more with longer period of measurement. The local electric field enhancement can lead to enlargement of electrical conductivity because of the electric field dependency of conductivity. This could cause more rapid charge carrier transport and help to limit the homo-polar space charge accumulation [30].

2.4. Dielectric spectroscopy

The dielectric spectroscopy was measured using an IMASS time-domain dielectric spectrometer (TDDS). A Laplace transformation was applied to the results to convert the data in the time domain to frequency response, as shown in Fig. 5. The real part (ε') of the relative permittivity denotes the charge accumulation, and the imaginary part (ε'') represents the loss in the polarization process. An evident bump in the spectroscopy of ε'' in the relatively high-frequency range for both EPDM1 and EPDM2 implies the existence of a loss peak. The loss peak can be attributed to the polarization of dipoles or bound charges. The frequencies of the bumps for EPDM2 are higher than those of EPDM1, suggesting that the relaxation speed of bound charges in EPDM2 is faster. At lower frequencies, the ε'' increases with the decrease of the frequency, and the slope of the spectroscopy in the log-log scale remains a constant, indicating the existence of a quasi-DC process [31].

Fundamentally, dielectric spectroscopy is the macroscopic response of charges to the applied electric field. To provide insights into the charge dynamics in the polarization processes, the Dissado-Hill dielectric response model is used to quantitatively analyze the dielectric spectroscopy. In the Dissado-Hill model, the concept of the cluster is utilized to characterize the charge dynamics. A cluster in the Dissado-Hill model can be considered as a spatially limited region with a partially regular structural order of individual units which are dynamically connected, e.g., inorganic fillers and their interface in this work. The loss peak is characterized by a complex susceptibility χ^* as a function of the angular frequency [32].

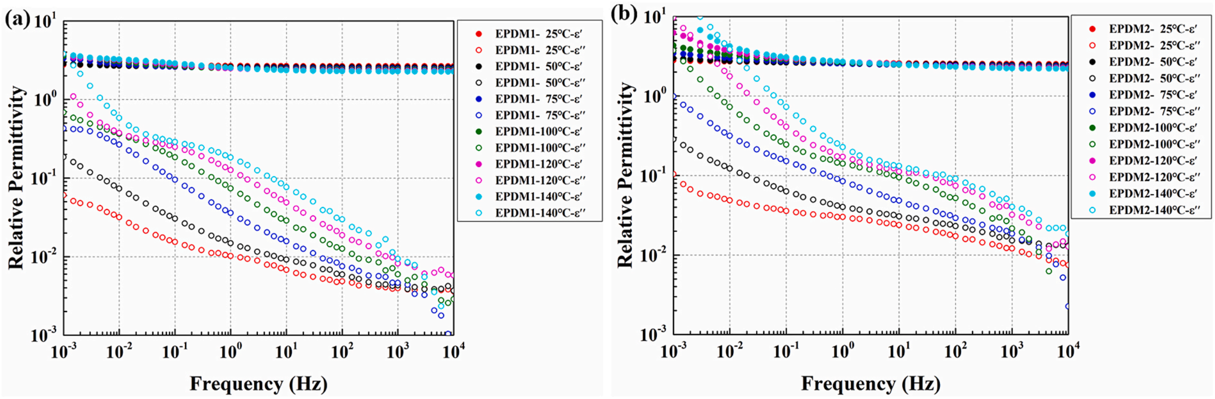

Fig. 5. Dielectric spectroscopy of (a) EPDM1 and (b) EPDM2. The relative permittivity is a dimensionless complex number expressed as $\varepsilon = \varepsilon'$-i$\varepsilon''$, where the real part ε' denotes the energy storage and the imaginary part ε'' denotes the energy loss in the polarization process.

$$\chi^*(\omega)=\chi_p\frac{\Gamma(1+m-n)}{\Gamma(2-n)\Gamma(m)}\left(1+i\frac{\omega}{\omega_p}\right)^{n-1}2F_1\cdot\left(1-n,1-m;2-n;\left(1+i\frac{\omega}{\omega_p}\right)^{-1}\right) \tag{2}$$

In equation (2), χ_p denotes the density of re-orientable dipoles (bound charges) per unit applied electric field, ω_p is the characteristic angular frequency denoting the rotational speed of the bound charges, and *m* and *n* denote the interaction of adjacent bound charges. Specifically, the exponent *n* defines the dynamic coupling of the bound charges within the cluster, and the exponent *m* defines the coupling of relaxations in one cluster with others. $\Gamma(x)$ is the Gamma function and $_2F_1$ (a, b; c; z) is the Gaussian hypergeometric function.

In the Dissado-Hill model, the weakly bound charges moving in the limited/restricted channels form the quasi-DC (Q-DC) process. The response function of the Q-DC process is expressed by equation (3) [31].

$$\chi^*(\omega)=\chi_c\frac{\Gamma(1-p-n)}{\Gamma(1-n)\Gamma(1-p)}\left(1+i\frac{\omega}{\omega_c}\right)^{n-1}\cdot 2F_1\left(1-n,1+p;2-n;\left(1+i\frac{\omega}{\omega_c}\right)^{-1}\right) \tag{3}$$

The χ_c denotes the density of weakly bound charges, the ω_c denotes the characteristic frequency at which the separation of the positive charge and its counter negative charge is equal to the size of the cluster. In the Q-DC process, the lowering of the frequency allows the opposite charges in the bound charge pairs to separate further and gives sufficient time for them to break apart and become independent. Once the reversal of the electric field direction is slow enough, i.e., to be less than the rate at which the bound charges separate, the response at frequencies below ω_c relates to charges that have separated. As the frequency reduces further, the charges have time to move apart further and thus generate a bigger dipole leading to the increase in the real part of the permittivity. As a result, the energy stored in the material is increased below ω_c. The parameters *p* and *n* denote the inter-cluster and intra-cluster interactions of charges.

There exists also a constant relative permittivity in ε' and a DC conductivity (s) in ε''. All these processes are combined in parallel, as shown by an equivalent circuit in Fig. 6. By fitting the total permittivity to the real part and imaginary part of the measured relative permittivity, parameters of all dielectric response processes can be calculated. As the dielectric spectroscopies at higher temperatures show higher accuracy, the characteristics of loss peaks and Q-DC processes can be better extracted from the modeling of results at higher temperatures. The calculated spectroscopies of all processes for EPDM1 and EPDM2 at 140 °C are illustrated in Fig. 7. Contributions of all processes at the frequency range investigated can be well observed from the calculated spectroscopies. The Loss Peak process appears in the relatively high frequency range. The peak frequency of EPDM1 is lower than 1 Hz, while it is close to the power frequency range for EPDM2. The Q-DC process dominated the responses in the relatively low frequency range in comparison to the Loss Peak process.

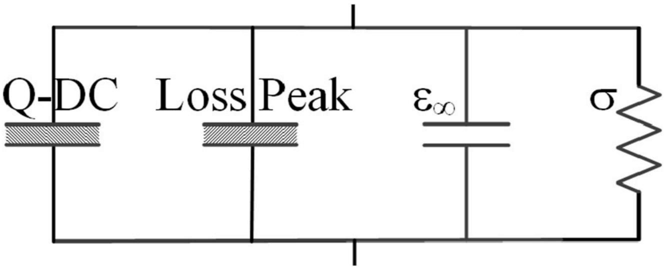

Fig. 6. Equivalent circuit of the EPDM composites for fitting the dielectric response data.

3. Discussion

3.1. Charge dynamics from dielectric spectroscopies and electrical conductivity

The Q-DC process is formed by the hopping of weakly bound charges in restricted paths. The weak physical bonding of inorganics and polymer chains in the interface region can provide such limited channels for charges to hop through [28,33,34]. As there is no obvious dipolar relaxation in the frequency range investigated, the loss peak is attributed to the strongly bound charge pairs, responding to the applied electric field. The calculated parameters of the Loss Peak process and the Q-DC process for EPDM1 and EPDM2 are summarized in Table 1. First of all, the characteristic frequency of the Loss Peak processes is higher than that of the Q-DC process. At higher frequencies, the transport charges in the Q-DC processes can be partly confined by the interface of inorganics temporarily, forming the bound charge pairs and the Loss Peak process [28,34]. As the frequency decreases, the trapped charges accumulate sufficient energies to escape from the interfacial traps, hopping in the form of a Q-DC process. Secondly, the amplitude of the Loss Peak process is lower than that of the Q-DC process, implying that the charges in the Q-DC transport process are partly trapped by the interface, forming the Loss Peak process.

Comparisons of dielectric spectroscopic parameters for EPDM1 and EPDM2 can provide quantitative information of charge dynamics. On one hand, the χ_p for EPDM1 is ~3 times of that for EPDM2, indicating that the trapping effects of the interface for Kaolinite particles are stronger than that of Talc particles. While the χ_c for EPDM2 is much higher than that of EPDM1, the even higher ratio of χ_p/χ_c further demonstrates the stronger trapping effects of the Kaolinite particles

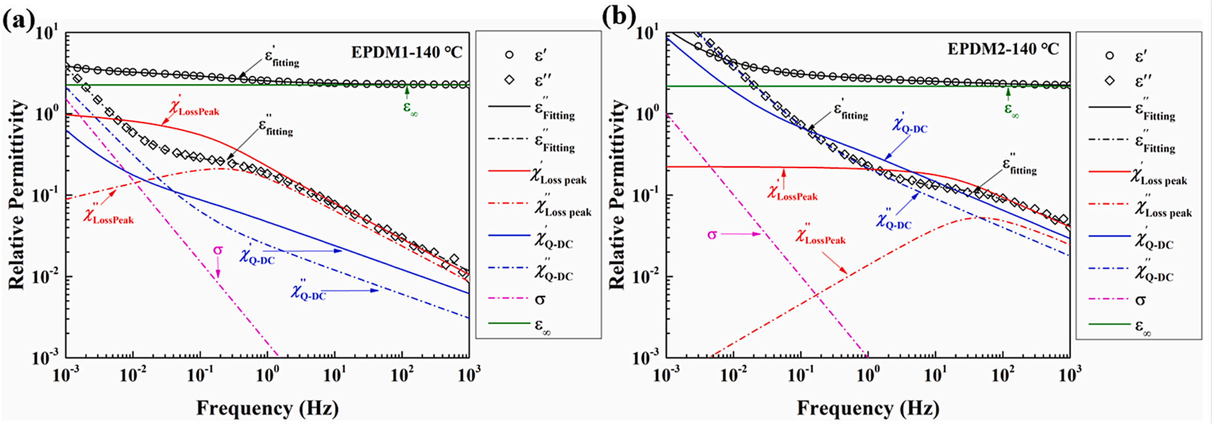

Fig. 7. Dielectric spectroscopies of different processes calculated from the Dissado-Hill model for (a) EPDM1 and (b) EPDM2.

Table 1
Parameters in the model for EPDM composites under 140 °C.

Sample	Loss Peak		Q-DC	
	χ_p	ω_p (rad/s)	χ_c	ω_c (rad/s)
EPDM1	0.122	2.32	0.173	0.87
EPDM2	0.042	218.54	0.728	2.16

Note: The parameters are defined in section 2.4.

interface. On the other hand, the ω_p of EPDM2 is almost two orders of magnitude higher than that of EPDM1, suggesting that the response of the trapped charges is more flexible for EPDM2. In addition, the higher ω_c of EPDM2 relative to EPDM1 indicates that in EPDM2 the time $(2\pi\omega_c{}^{-1})$ for charges and their counter charges to be separated to a distance equivalent to the size of the filler is shorter. The shorter time means the transport of charges is easier for EPDM2. The less restriction to the relaxation of trapped charges and to the transport of movable charges in EPDM2 are beneficial to suppress the space charge accumulation.

The charge relaxation and transport dynamics achieved from the dielectric spectroscopy and Q-DC analysis can also be supported and validated by the DC electrical conductivity. The observed electrical conductivity is the result of both electronic and ionic charge transport under DC electric field. In comparison to EPDM1, EPDM2 with Talc 2D-nanoclay particles has higher conductivity in all the measured temperatures and electric fields. The higher conductivity is attributed to the higher mobility of charge carriers in EPDM2 compared with EPDM1. The calculated activation energies and electrical conductivities at infinite temperature are summarized in Table 2. The activation energy can be considered as the energy barrier against charge carriers to move under the electric field. Therefore, the notably lower activation energy of EPDM2, 0.45 eV, compared with EPDM1, 0.95 eV, suggests that the charge carriers in EPDM2 with Talc 2D-nanoclay particles confront less hindrance to transfer between the localized states and the particles. In addition, the amount of electrical conductivity at infinite temperature, σ_0, gives some idea about the condition that all the charge carriers could be de-trapped and hopped between the localized states and the particles. The significant difference in the amount of σ_0 implies the higher amount of charge carriers trapped or restricted in EPDM1 which can be involved in hopping at infinite temperature.

Table 2
The fitted parameters of the Arrhenius function for EPDM composites at 10 kV/mm.

Sample	Electrical conductivity at infinite temperature σ_0 (S/m)	Activation energy φ (eV)
EPDM1	1.81×10^{2}	0.95
EPDM2	2.08×10^{-7}	0.45

3.2. Charge dynamics description

In EPDM1, the 2D-nanoclay particles aggregated and formed bulb-like particles causing the composite dielectric not having suitable quality in terms of electrical properties. In this condition, the average distance between the aggregated particles with the same weight ratio concentration is higher and the average size of the particles is larger compared with the uniform distribution of the particles. In addition, the aggregation decreases the total surface area and thus reduces the interfacial region, compromising the interactions of polymer and the inorganic particles. In contrast, EPDM2 with the great electrical performance for DC insulation has a uniform distribution of the 2D-nanoclays in the polymer matrix with a preferred orientation of 2D platelet-like nanoclays parallel with the surface of the film sample confirmed with the X-ray pole figure technique. Free from agglomeration, this can lead to the shortened average distance between the particles or stacks of the particles in the range of nanometer. To have a uniform distribution of the 2D-nanoclay particles and be free from agglomeration, the clay particles with low cation exchange capability (CEC) [35] such as Kaolinite [36] and Talc [37] are desired. The CEC of Talc particles, 0.2 (meq/100 g), is significantly smaller than that of Kaolinite, ~3–15 (meq/100 g) [38] which means that the stacks of clay particles in EPDM1 have a higher tendency to hold tightly together and build aggregated micro particles. This explains the aggregation of the Kaolinite 2D-nanoclay particles in EPDM1 which results in the formation of the bulb-like micro particles in the polymer matrix compared with the uniform distribution of the Talc 2D-nanoclays.

Considering a uniform and oriented distribution of 2D-nanoclays in a cross-linked amorphous polymer matrix as schemed in Fig. 8, the distance between 2D-nanoclays filled with polymer matrix can be divided into two layers. The first layer is the interface of the inorganic nanoclay particles with organic polymer matrix. This layer includes all the possible functionalized groups as the surface treatment and coupling agents which adhere to both the organic polymer chain and the surface of inorganic particles due to different functional groups [39,40]. In this layer, through ionic, covalent, and hydrogen bonds or van der Waals force, the organic polymer chains are connected to the inorganic nanoclay particles. The second layer includes the distributed and twisted cross-linked polymer chains with (constrained) free volume. The characteristics related to the polymer matrix such as crystalline morphology, the density of cross-linking, as well as the density and mobility of the polymer chains are related to this layer [41]. This layer is characterized by having localized energy states in the polymer chains as the path of electronic conduction and having free volume as the conduction path for

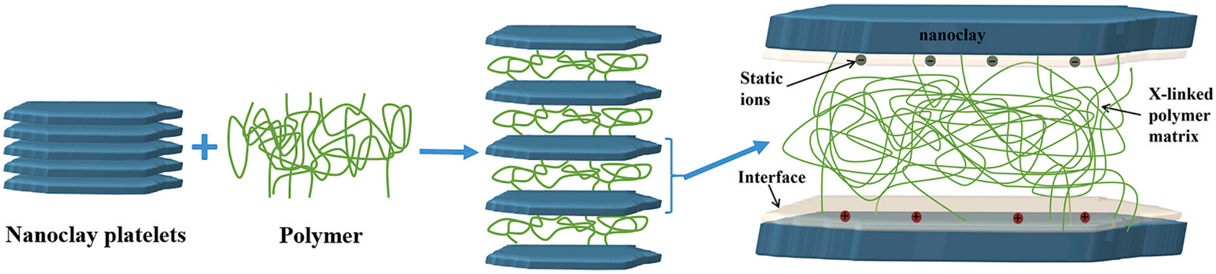

Fig. 8. Scheme of the space between the well-oriented 2D platelet-like nanoclays.

ionic conduction.

Charge dynamics in the polymer/2D-nanoclays dielectrics comprise both electronic and ionic conductions. The source of electronic charge carriers, i.e., electrons and holes, in composite dielectrics can be related to charge injection phenomena, such as Schottky injection [42] or Fowler-Nordheim tunneling [43] at the electrode-dielectric interface, as well as the donor states with a process like Poole-Frenkel in the bulk [44]. The electronic charge transport in wide bandgap polymeric dielectrics can be described by the Multiple-trapping model in which the charges captured by localized states are released and transfer in extended states located above the mobility edge [45–47]. During the transfer in the extended states, the charges may be trapped again by the localized states. This can happen many times before the charges leave the dielectric [49]. Therefore, the electrical conductivity is in relation with the difference of the mobility edge, E_c, and the energy level of the localized states, E_t, as presented in (4) [45];

$$\sigma \propto exp\left(-\left(E_c - E_t\right)/kT\right) \quad (4)$$

where E_c - E_t is the activation energy. As a result, the shallower localized states enhance the electrical conductivity.

The presence of the localized states in dielectrics can be attributed to defects such as structural disorder, chemical impurities, and interfacial effects [45]. The defects cause a distribution for the localized states between the highest occupied molecular orbitals (HOMO) and the lowest unoccupied molecular orbitals (LUMO) in the polymer chain. The presence of nanoclay particles in the polymer matrix can introduce new localized states or modify the available localized states. The introduction of the new localized states is the reason for enhanced electrical conductivity in composite dielectrics compared with the pure polymer. The difference in the energy levels and bandgaps of the polymer matrix and the nanoclay particles is one of the main reasons for the formation of the localized states [46]. The larger the difference between the bandgap of polymer matrix and nanoparticle, the deeper the introduced localized states are. The Kaolinite particles with a bandgap of 4.52 eV [48], compared with 5.3 eV bandgap for Talc particles [49], have the higher bandgap difference with the bandgap of EPDM polymer chain which is ~6–7 eV [50]. This larger bandgap difference for Kaolinite particles increases the possibility of the introduction of deep localized states to the polymer chain in EPDM1. The deep localized states can act as deep traps which enhance the possibility of capturing the electronic charge carriers when they transfer under electric field and thermal activation. The possible presence of the deep localized states in EPDM1 can be the reason for the higher amount of the charge accumulation in EPDM1 at both 25 °C and 50 °C with TG compared with EPDM2. Additionally, the larger interfacial area leads to more interaction zone between the nanoclays and the polymer chains. The interfacial area can interact with the available localized states electrostatically because of the far-distance effect and modify the localized states to the shallower ones [41]. The larger interfacial area between the polymer matrix and the 2D platelet-like nanoclays of Talc in EPDM2, in comparison to the aggregated bulb-like particles of Kaolinite, results in the larger interaction zone. The higher interfacial area can enlarge the density of the shallow localized states which control the electronic charge transport under electric field and cause the higher electrical conductivity of EPDM2, compared with EPDM1.

The other part of charge carriers' movement in composite dielectrics especially under low electric fields is related to ionic conduction [20]. The ions can be produced under electric field and thermal activation by chemical reactions such as reactions involving antioxidants, dissociation of impurities or absorbed water, electrochemical reactions at the electrode-dielectric interfaces, etc. [51,52]. Under electric field and thermal activation, the slow mobile ions move (hop) between the particles, contributing to the ionic conduction. The movement of ions is nonlinear, and it is more twisted and windy due to the restrictions such as constrained free volume and configuration of the polymer chain [20]. Because of the distribution of nanoparticles in the polymer matrix and intrinsic heterogeneity of the composite dielectrics, ionic-interfacial polarization or Maxwell-Wagner (MW) effect under DC electric field is expected [53,54]. The ionic-interfacial polarization causes a built-up of charge at the interface of the nanoparticles and the polymer matrix. When the distance between the nanoclay particles is sufficiently short, the slow ions can hop between the nanoparticles easily and reach the next nanoparticle. Each of the nanoclay particles can act as a recombination center because the charge build-up on the surface of nanoclay particles due to the MW effect can neutralize the mobile ions under the electric field. The uniform and oriented distribution of 2D-nanoclays in EPDM2 contribute to the nanometric distance between the particles, and thus the ions can reach the next particles and be neutralized with higher possibility. Besides, the large interfacial area of the 2D-nanoclays in EPDM2 enhances the possibility of neutralizing ions due to the larger interaction zones between the mobile ions and the built-up charge around the particles. In contrast, the higher average distance between the particles and the smaller total interfacial area in EPDM1 when compared with EPDM2 enhance the possibility of trapping charge around the bulb-like particles which act as the potential wells causing charge accumulation.

The calculated activation energies confirm the lower restrictions against charge carriers' transport in EPDM2, compared with EPDM1. Moreover, the Q-DC analysis supports that in the composite dielectric with aggregation of particles, EPDM1, it is harder for the trapped charge to move, resulting in higher density of the trapped charge. In contrast, from Q-DC analysis, the mobility of charge carriers for hopping between the particles is higher in EPDM2 with the uniform distribution of 2D-nanoclay particles.

4. Conclusion

The EPDM-base composite dielectrics with two different 2D-nanoclays including Kaolinite and Talc were fabricated and studied. The composite dielectric with Kaolinite showed a notable space charge accumulation which consequently caused electric field distortion across the sample up to 59.5% at 50 °C with thermal gradient (TG). On the other hand, the space charge was suppressed significantly in composite dielectrics with Talc nanoparticles and the electric field distortion decreased to 9% at the same condition. Based on the experimental results and with the application of the well-known models, a mechanism discussion was put forward regarding the charge transport and accumulation in composite dielectrics. Our discussion suggests the larger interfacial area between the polymer matrix and the particles causes higher electrical conductivity due to the higher density of the shallow localized states. Additionally, the lower difference between the bandgap of the polymer chains and the particles results in the less possibility of charge accumulation during electronic charge transport due to the lower density of the deep localized states. The uniform and oriented distribution of 2D platelet-like Talc particles, the large interfacial area of the nanoclay particles, and the shorter average distance between the particles reduce the possibility of trapping charge carriers in the neighborhood of particles during the ionic charge transport. The charge dynamics using the Dissado-Hill model analysis verified the higher mobility and the weaker trapping effect in the composite dielectric with the uniform and oriented distribution of the Talc 2D-nanoclay particles.

Declaration of competing interest

The authors declare the following financial interests/personal relationships which may be considered as potential competing interests:

Yang Cao reports financial support was provided by the National Science Foundation for partial funding support under Grant No. 1650544.

Acknowledgements

The authors would like to thank Kerite, Okonite, Electrical Cable Compounds, Lion Elastomers, and Exxon Mobil for sponsoring the research and the National Science Foundation for partial funding support under Grant No. 1650544 through the NSF Industrial University Collaborative Research Center on High Voltage/Temperature Materials and Structures (NSF iUCRC HVT). The authors also would like to thank JoAnne Ronzello, Dr. Mattewos Tefferi, Dr. Chuanyang Li, Tohid Shahsavrian, Dr. Chris Calebrese, Dr. Daniela Morales for their help for this study.

References

[1] Global Wind Energy Council, https://gwec.net/gwec-offshore-wind-will-surge-to-over-234-gw-by-2030-led-by-asia-pacific/(accessed 5 August 2020).

[2] E. Prieto-Araujo, O. Gomis-Bellmunt, Wind turbine technologies, in: D.V. Hertem, O. Gomis-Bellmunt, J. Liang (Eds.), HVDC Grids: for off- Shore and Supergrid of the Future, Piscataway, NJ, 2016, pp. 97–108.

[3] D. Fabiani, G.C. Montanari, C. Laurent, G. Teyssedre, P.H.F. Morshuis, R. Bodega, L.A. Dissado, HVDC cable design and space charge accumulation. Part 3: effect of temperature gradient, IEEE Electr. Insul. Mag. 24 (2008) 5–14, https://doi.org/10.1109/MEI.2008.4473049.

[4] R.L. Sellick, J.S. Sullivan, Q. Chen, C. Calebrese, Future improvements to HVDC cables through new cable insulation materials, in: 13th IET International Conference on AC and DC Power Transmission, ACDC, 2017, https://doi.org/10.1049/cp.2017.0039.

[5] P. Cox, R. Fleming, F. Krajick, S. Boggs, Y. Cao, AC and impulse performance of medium voltage ethylene propylene- rubber cables with over 25 years of in-service aging in a wet underground environment, IEEE Electr. Insul. Mag. 32 (2016) 24–28, https://doi.org/10.1109/MEI.2016.7527122.

[6] X. Qi, S. Boggs, Thermal and mechanical properties of EPR and XLPE cable compounds, IEEE Electr. Insul. Mag. 22 (2006) 19–24, https://doi.org/10.1109/MEI.2006.1639026.

[7] M.A. Baferani, C. Li, M. Tefferi, N. Wang, Y. Cao, Large Improvement in DC electrical properties of EPDM with 2D platelet nanoclay, J. Phys. D Appl. Phys. 54 (2021), https://doi.org/10.1088/1361-6463/ac2277.

[8] M. Tefferi, Z. Li, Y. Cao, H. Uehara, Q. Chen, Novel EPR-insulated DC cables for future multi-terminal MVDC integration, IEEE Electr. Insul. Mag. 35 (2019) 20–27, https://doi.org/10.1109/MEI.2019.8804331.

[9] B. Li, P.I. Xidas, E. Manias, High breakdown strength polymer nanocomposites based on the synergy of nanofiller orientation and crystal orientation for insulation and dielectric applications, ACS Appl. Nano Mater. 1 (2018) 3520–3530, https://doi.org/10.1021/acsanm.8b00671.

[10] B. Li, P.I. Xidas, K.S. Triantafyllidis, E. Manias, Effect of crystal orientation and nanofiller alignment on dielectric breakdown of polyethylene/montmorillonite nanocomposites, Appl. Phys. Lett. 111 (2017), 082906, https://doi.org/10.1063/1.4996717.

[11] C.G. Ma, Y.L. Mai, M.Z. Rong, W.H. Ruan, M.Q. Zhang, Phase structure and mechanical properties of ternary polypropylene/elastomer/nano-$CaCO_3$ composites, Compos. Sci. Technol. 67 (2007) 2997–3005, https://doi.org/10.1016/j.compscitech.2007.05.022.

[12] O. Zabihi, M. Ahmadi, S. Nikafshar, K.C. Preyeswary, M. Naebe, A technical review on epoxy-clay nanocomposites: structure, properties, and their applications in fiber reinforced composites, Compos. B Eng. 135 (2018) 1–24, https://doi.org/10.1016/j.compositesb.2017.09.066.

[13] T. Takada, Y. Hayase, Y. Tanaka, T. Okamoto, Space charge trapping in electrical potential well caused by permanent and induced dipoles for LDPE/MgO nanocomposite, IEEE Trans. Dielectr. Electr. Insul. 15 (2008) 152–160, https://doi.org/10.1109/T-DEI.2008.4446746.

[14] L. Zhang, M.M. Khani, T.M. Krentz, Y. Huang, Y. Zhou, B.C. Benicewicz, L. S. Schadler, Suppression of space charge in crosslinked polyethylene filled with poly (stearyl methacrylate)-grafted SiO_2 nanoparticles, Appl. Phys. Lett. 110 (2017), 132903, https://doi.org/10.1063/1.4979107.

[15] R. Liao, J. Wang, F. Gao, Y. Yuan, Z. Xu, Effects of aluminum nitride nanoparticles on the space charge behavior of cellulose paper, J. Mater. Sci. 51 (2016) 10701–10713, https://doi.org/10.1007/s10853-016-0196-x.

[16] X. Huang, J. Pingkai, Y. Yi, Nanoparticle surface modification induced space charge suppression in linear low density polyethylene, Appl. Phys. Lett. 95 (2009), 242905, https://doi.org/10.1063/1.3275732.

[17] J. Zhao, Z. Xu, G. Chen, P.L. Lewin, Numeric description of space charge in polyethylene under ac electric fields, J. Appl. Phys. 108 (2010), 124107, https://doi.org/10.1063/1.3524433.

[18] F. Boufayed, G. Teyssedre, C. Laurent, S. Le Roy, L.A. Dissado, P. Ségur, G. C. Montanari, Models of bipolar charge transport in polyethylene, J. Appl. Phys. 100 (2006), 104105, https://doi.org/10.1063/1.2375010.

[19] T.J. Lewis, Interfaces are the dominant feature of dielectrics at the nanometric level, IEEE Trans. Dielectr. Electr. Insul. 11 (2004) 739–753, https://doi.org/10.1109/TDEI.2004.1349779.

[20] T. Tanaka, M. Kozako, N. Fuse, Y. Ohki, Proposal of a multi-core model for polymer nanocomposite dielectrics, IEEE Trans. Dielectr. Electr. Insul. 12 (2005) 669–681, https://doi.org/10.1109/TDEI.2005.1511092.

[21] S. Singha, M.J. Thomas, Dielectric properties of epoxy nanocomposites, IEEE Trans. Dielectr. Electr. Insul. 15 (2008) 12–23, https://doi.org/10.1109/T-DEI.2008.4446732.

[22] S. Li, G. Yin, G. Chen, J. Li, S. Bai, L. Zhong, Y. Zhang, Q. Lei, Short-term breakdown and long-term failure in nanodielectrics: a review, IEEE Trans. Dielectr. Electr. Insul. 17 (2010) 1523–1535, https://doi.org/10.1109/TDEI.2010.5595554.

[23] T. Andritsch, R. Kochetov, B. Lennon, P.H.F. Morshuis, J.J. Smit, Space charge behavior of magnesium oxide filled epoxy nanocomposites at different temperatures and electric field strengths, in: Electrical Insulation Conference, EIC, 2011, https://doi.org/10.1109/EIC.2011.5996133.

[24] T. Tanaka, A quantum dot model for permittivity of polymer nanocomposites, in: IEEE Conference on Electrical Insulation and Dielectric Phenomena, CEIDP, 2016, https://doi.org/10.1109/CEIDP.2016.7785454.

[25] K. Inaba, S. Kobayashi, Various pole figure measurement techniques with SmartLab, assisting thin film characterization, Rigaku J. 34 (2018) 10–16.

[26] G. Teyssedre, C. Laurent, Charge transport modeling in insulating polymers: from molecular to macroscopic scale, IEEE Trans. Dielectr. Electr. Insul. 12 (2005) 857–875, https://doi.org/10.1109/TDEI.2005.1522182.

[27] M.A. Baferani, C. Li, T. Shahsavarian, J. Ronzello, Y. Cao, Y, High temperature insulation materials for DC cable insulation—Part I: space charge and conduction, IEEE Trans. Dielectr. Electr. Insul. 28 (2021) 223–230, https://doi.org/10.1109/TDEI.2020.009167.

[28] C. Wu, M. Arab, J. Ronzello, Y. Cao, Charge transport dynamics and space charge accumulation in XLPE composites with 2D platelet fillers for HVDC cable insulation, IEEE Trans. Dielectr. Electr. Insul. 28 (2021) 3–10, https://doi.org/10.1109/TDEI.2020.008948.

[29] H. Uehara, Z. Li, Q. Chen, G.C. Montanari, Y. Cao, Space charge behavior under thermal gradient in cross-linked polyethylene and ethylene-propylene rubber, Sensor. Mater. 29 (2017) 1199–1212, https://doi.org/10.18494/SAM.2017.1538.

[30] L.A. Dissado, The role of theory in understanding space charge distributions, in: 2020 International Symposium on Electrical Insulating Materials, ISEIM), 2020, pp. 1–14.

[31] L.A. Dissado, R.M. Hill, Anomalous low-frequency dispersion. Near direct current conductivity in disordered low-dimensional materials, J. Chem. Soc., Faraday Trans. 2: Mol. Chem. Phys. 80 (1984) 291–319, https://doi.org/10.1039/F29848000291.

[32] L.A. Dissado, R.M. Hill, A cluster Approach to the structure of imperfect materials and their relaxation spectroscopy, Proc. Roy. Soc. Lond. A. Math. Phys. Sci. 390 (1983), https://doi.org/10.1098/rspa.1983.0125.

[33] Y. Gao, X. Liang, L.A. Dissado, S.J. Dodd, N.M. Chalashkanov, Dielectric response of filled high temperature vulcanized silicone rubber, IEEE Trans. Dielectr. Electr. Insul. 23 (2016) 3683–3695, https://doi.org/10.1109/TDEI.2016.006057.

[34] C. Wu, X. Liang, L.A. Dissado, N.M. Chalashkanov, S.J. Dodd, Y. Gao, S. Xu, Dielectric response of nano aluminium tri-hydrate filled silicone rubber, Compos. Sci. Technol. 163 (2018) 56–62, https://doi.org/10.1016/j.compscitech.2018.04.002.

[35] H. Shi, T. Lan, T.J. Pinnavaia, Interfacial effects on the reinforcement propertiesof polymer-organoclay nanocomposites, Chem. Mater. 8 (1996) 1584–1587, https://doi.org/10.1021/cm960227m.

[36] G.E. Christidis, P. Makri, V. Perdikatsis, Influence of grinding on the structure and colour properties of talc, bentonite and calcite white fillers, Clay Miner. 39 (2004) 163–175, https://doi.org/10.1180/0009855043920128.

[37] N. Chaikum, N. Sooppipatt, R.M. Carr, The cation exchange capacity of some Kaolin minerals, J. Sci. Soc. Thail. 7 (1989) 100–109, https://doi.org/10.2306/scienceasia1513-1874.1981.07.100.

[38] D. Carroll, Ion exchange in clays and other minerals, Geol. Soc. Am. Bull. 70 (1959) 749–779, https://doi.org/10.1130/0016-7606(1959)70[749:ieicao]2.0.co;2.

[39] Y. Xie, C.A. Hill, Z. Xiao, H. Militz, C. Mai, C, Silane coupling agents used for natural fiber/polymer composites: a review, Compos. Appl. Sci. Manuf. 41 (2010) 806–819.

[40] M.Z. Rong, M.Q. Zhang, W.H. Ruan, Surface modification of nanoscale fillers for improving properties of polymer nanocomposites: a review, Mater. Sci. Technol. 22 (2006) 787–796, https://doi.org/10.1179/174328406X101247.

[41] T. Tanaka, Dielectric nanocomposites with insulating properties, IEEE Trans. Dielectr. Electr. Insul. 12 (2005) 914–928, https://doi.org/10.1109/TDEI.2005.1522186.

[42] G. Simmons, Richardson-Schottky effect in solids, Phys. Rev. Lett. 15 (1965) 25, https://doi.org/10.1103/PhysRevLett.15.967.

[43] W.C. Lee, C. Hu, Modeling CMOS tunneling currents through ultrathin gate oxide due to conduction-and valence band electron and hole tunneling, IEEE Trans. Electron. Dev. 48 (2001) 1366–1373, https://doi.org/10.1109/16.930653.

[44] F.C. Chiu, A review on conduction mechanisms in dielectric films, Adv. Mater. Sci. Eng. (2014), 578168, https://doi.org/10.1155/2014/578168, 2014.

[45] G. Blaise, Charge localization and transport in disordered dielectric materials, J. Electrost. 50 (2001) 69–89, https://doi.org/10.1016/S0304-3886(00)00027-9.

[46] H.F. Haneef, A.M. Zeidell, O.D. Jurchescu, Charge carrier traps in organic semiconductors: a review on the underlying physics and impact on electronic devices, J. Mater. Chem. C 8 (2020) 759–787, https://doi.org/10.1039/C9TC05695E.

[47] G. Horowitz, Validity of the concept of band edge in organic semiconductors, J. Appl. Phys. 118 (2015), 115502, https://doi.org/10.1063/1.4931061.

[48] Ly Xia, H. Zhong, Gy Liu, Xg Li, Electron band structure of kaolinite and its mechanism of flotation using dodecylamine as collector, J. Cent. South Univ. Technol. 16 (2009) 73–79, https://doi.org/10.1007/s11771-009-0012-8.

[49] A.B. Alencar, A.P.M. Barboza, B.S. Archanjo, H. Chacham, B.R. Neves, Experimental and theoretical investigations of monolayer and few-layer talc, 2D Mater. 2 (2015), 015004, https://doi.org/10.1088/2053-1583/2/1/015004.

[50] J. Li, B. Du, J. Su, H. Liang, Y. Liu, Surface layer fluorination-modulated space charge behaviors in HVDC cable accessory, Polymers 10 (2018) 500, https://doi.org/10.3390/polym10050500.

[51] M. Pollak, B. Shklovskii, Hopping Transport in Solids, first ed.s., Elsevier, North Holland, 1991.

[52] R. Edward Barker Jr., Mobility and conductivity of ions in and into polymeric solids, Macromol. Chem. 11 (1977) 157–170, https://doi.org/10.1016/B978-0-08-020975-3.50011-6.

[53] A.R.V. Hippel, Dielectrics and Waves, MA: M. I. T. Press, Cambridge, 1954.

[54] T.W. Dakin, Conduction and polarization mechanisms and trends in dielectric, IEEE Electr. Insul. Mag. 22 (2006) 11–28, https://doi.org/10.1109/MEI.2006.1705854.